Formation of the Lunar Fossil Bulges and Its Implication for the Early Earth and Moon

Chuan Qin[1,2] (ID), Shijie Zhong[1] (ID), and Roger Phillips[3] (ID)

[1]Department of Physics, University of Colorado Boulder, Boulder, CO, USA, [2]Now at Department of Earth and Planetary Sciences, Harvard University, Cambridge, MA, USA, [3]Department of Earth and Planetary Sciences and McDonnell Center for the Space Sciences, Washington University, St. Louis, MO, USA

Abstract First recognized by Laplace over two centuries ago, the Moon's present tidal-rotational bulges are significantly larger than hydrostatic predictions. They are likely relics of a former hydrostatic state when the Moon was closer to the Earth and had larger bulges, and they were established when stresses in a thickening lunar lithosphere could maintain the bulges against hydrostatic adjustment. We formulate the first dynamically self-consistent model of this process and show that bulge formation is controlled by the relative timing of lithosphere thickening and lunar orbit recession. Viable solutions indicate that lunar bulge formation was a geologically slow process lasting several hundred million years, that the process was complete about 4 Ga when the Moon-Earth distance was less than ~32 Earth radii, and that the Earth in Hadean was significantly less dissipative to lunar tides than during the last 4 Gyr, possibly implying a frozen hydrosphere due to the fainter young Sun.

1. Introduction

The Moon's tidal-rotational bulges are abnormally larger than predicted from the hydrostatic theory for the present-day lunar rotational and orbital states, as has been recognized for over two centuries (Laplace, 1798). The most recent measurement by Gravity Recovery and Interior Laboratory mission showed that the (unnormalized) spherical harmonic degree 2 coefficients of the Moon's gravitational anomalies, C_{20} and C_{22}, which characterize the size of the bulges, are -2.03×10^{-4} and 2.23×10^{-5}, respectively (Zuber et al., 2013), and they are about 22 and 8 times larger than their corresponding hydrostatic values (Garrick-Bethell et al., 2014; Keane & Matsuyama, 2014). After correcting for the effects from large basins and true polar wander, C_{20} and C_{22} become -1.56×10^{-4} and 3.88×10^{-5}, respectively, and remain about 17 and 14 times their corresponding hydrostatic values (Keane & Matsuyama, 2014).

The prevalent hypothesis for the Moon's excess bulge is that it is a remnant feature, called a fossil bulge, "frozen in" from an early Moon that had a larger bulge because the Moon was closer to the Earth, spun faster, and experienced larger rotational and tidal forces (e.g., Jeffreys, 1915; Lambeck & Pullan, 1980; Sedgwick, 1898). As the Moon receded from the Earth due to Earth's tidal dissipation, it cooled to form a strong outer layer (i.e., lithosphere) that thickened with time, and the early bulge might have been partially to fully retained against hydrostatic adjustment (Jeffreys, 1915; Lambeck & Pullan, 1980; Sedgwick, 1898). The corrected C_{20} and C_{22} values are consistent with the fossil bulges formed on a synchronous lunar orbit with small eccentricity (Keane & Matsuyama, 2014) (Figure 1a). Previous studies have considered a variety of complicating factors including nonzero eccentricity and nonsynchronous spin-orbit resonances (e.g., Garrick-Bethell et al., 2006) and suggested that the bulges might have formed when the lunar orbit semimajor axis a ranged from 15 R_E to 32 R_E (e.g., Garrick-Bethell et al., 2014; Keane & Matsuyama, 2014; Lambeck & Pullan, 1980; Matsuyama, 2013) (R_E is the Earth's radius) or 200–300 Myr after lunar accretion (Garrick-Bethell et al., 2014). However, these estimates were based on models that either ignored elastic lithosphere or considered elastic lithosphere that is formed instantaneously with a constant thickness and did not take into account the time-dependent processes that are important for fossil bulge formation.

The development of the fossil bulge is a continuous dynamic process. To describe the dynamics of bulge formation, a method that incorporates viscoelastic rheology with time-dependent tidal-rotational forces and lithosphere thickening due to cooling is needed. Such modeling presents challenges to conventional computational techniques that are mostly applicable to problems with either time-invariant viscoelastic
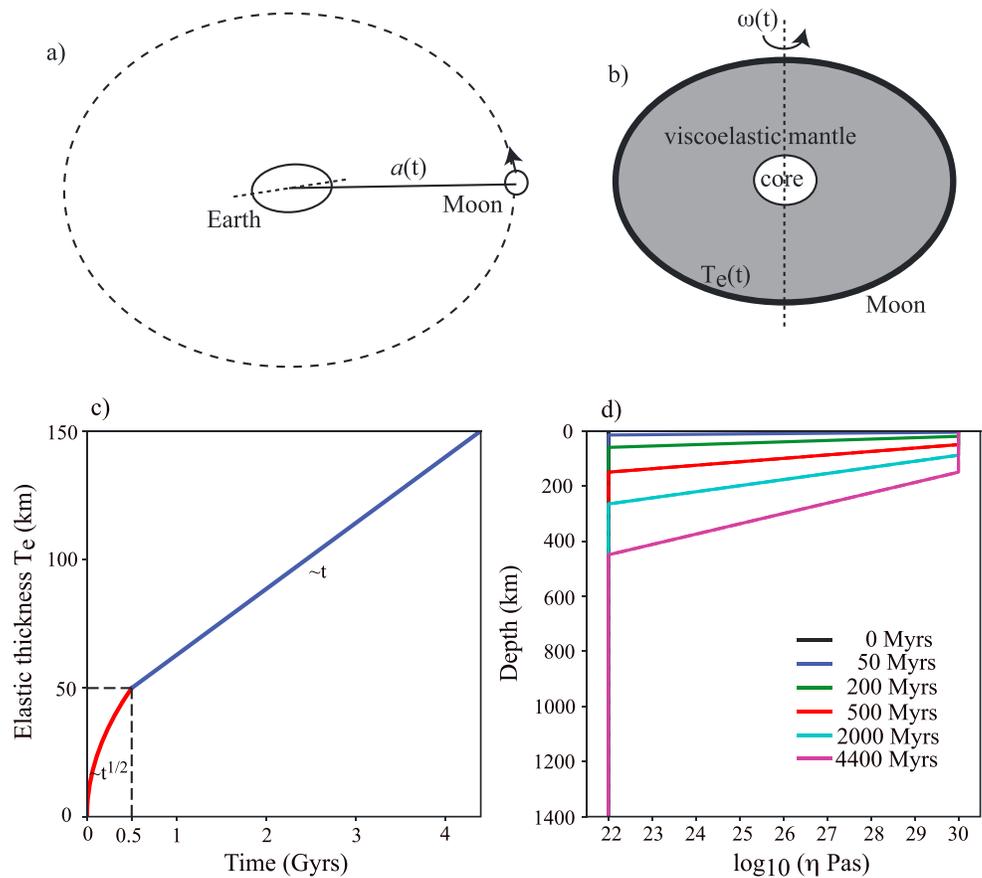
Figure 1. The model for the lunar fossil bulge formation and the Earth-Moon system. (a) The semimajor axis of the lunar orbit a increases with time t, due to the tidal dissipation of the Earth that causes angular momentum transfer and Moon's recession. (b) The model for the lunar fossil bulge formation with an elastic lithosphere of thickness T_e and the mantle overlying a core. (c) Time evolution of T_e for a reference model. Our model does not consider the lunar magma ocean era that may last for ~100 Myr (Elkins-Tanton et al., 2011) with negligibly small T_e. (d) Depth-dependent viscosity at different times. See section 2 for model details.

properties (e.g., Tromp & Mitrovica, 1999) or relatively short timescales (Zhong et al., 2003). In this study, by employing a semianalytical computational method (Text S1 in the supporting information), we illustrate the development of lunar fossil bulges with time and determine how the size of the bulges depends on the Moon's orbit evolution and cooling history. Since the lunar orbital evolution is largely controlled by tidal dissipation of the Earth, that is, its Q value (e.g., Lambeck & Pullan, 1980), our study may provide constraints on the dynamics of the early Earth and Moon, based on the observation of the lunar fossil bulge.

2. Models and Methods

We present the first dynamically self-consistent model for lunar fossil bulge development, in which we consider a viscoelastic Moon that is subject to long-term (~4 Gyr) change of tidal-rotational state and viscoelastic structure (Figure 1). Here we show and discuss the governing equations, the models for lunar mantle rheology and lunar orbital evolution, and our computational method.

2.1. Governing Equations

We consider the Moon's mantle as a viscoelastic spherical shell that deforms in response to time-dependent tidal-rotational potential or force (Figure 1). The time-evolving surface deformation or the "bulge" formation can be solved by the conservation equations of mass and momentum. By assuming an incompressible,

viscoelastic, and self-gravitating lunar mantle, the two governing equations are expressed (Zhong et al., 2003), respectively, as

$$\nabla \cdot \boldsymbol{u} = 0, \tag{1}$$

$$\nabla \cdot \boldsymbol{\sigma} + \rho_0 \nabla \varphi + \rho_0 \nabla V - \rho_1^E \boldsymbol{g} - \nabla(\rho_0 g u_r) = 0, \tag{2}$$

together with the Poisson's equation

$$\nabla^2 \varphi = -4\pi G \rho_1^E, \tag{3}$$

where $\boldsymbol{u}$ is the displacement vector with u_r being in the radial direction, φ is the gravitational potential due to deformation, V is the applied potential (e.g., rotational and tidal potentials), $\boldsymbol{\sigma}$ is the stress tensor, ρ_0 is the density and is constant due to incompressibility, $\boldsymbol{g}$ is the gravitational acceleration of the Moon, $\rho_1^E = -\nabla \cdot (\rho_0 \boldsymbol{u})$ is the Eulerian density perturbation, and G is the gravitational constant.

The core-mantle boundary (CMB) has a radius of 340 km (Weber et al., 2011) with a liquid and self-gravitating core, and the surface is at the lunar radius of 1,740 km. Stress-free boundary conditions are applied to the surface and CMB such that both boundaries can deform in response to the applied potential and the gravitational potential associated with mass anomalies of the boundary displacement. By solving the governing equations under the given boundary conditions and for certain rheological models and applied potential V, we determine the displacement, gravitational anomalies, and stress for the Moon. The surface displacement and gravitational anomalies are then compared with the observed lunar bulge.

2.2. Rheological Models and Lithospheric Thickening With Time

We adopt a simple Maxwellian rheology (i.e., elastic and viscous strains are additive) (Zhong et al., 2003) to describe the viscoelasticity of the lunar mantle and lithosphere, which is given by

$$\boldsymbol{\sigma} + \frac{\eta}{\mu}\dot{\boldsymbol{\sigma}} = -\left(P + \frac{\eta}{\mu}\dot{P}\right)\boldsymbol{I} + 2\eta\dot{\boldsymbol{\varepsilon}}, \tag{4}$$

where $\boldsymbol{\varepsilon}$ is the strain and $\boldsymbol{\varepsilon} = \frac{1}{2}(\nabla \boldsymbol{u} + \nabla^T \boldsymbol{u})$, P is the pressure, μ is the shear modulus, η is the viscosity, and the dot denotes time derivative. For our incompressible viscoelastic model, the lunar mantle density and shear modulus are taken as constants 3,400 kg/m³ and 6.5×10^{10} Pa, respectively, consistent with the values inferred from seismic studies (Weber et al., 2011).

The viscosity depends strongly on temperature and hence the lunar thermal history. Given the important role of the lithosphere in supporting the bulges (Lambeck & Pullan, 1980; Zhong & Zuber, 2000) and the uncertainties in lunar thermal evolution and mantle rheology, we use a thickening elastic lithosphere with a thickness T_e as a surrogate for the viscosity evolution as the Moon cools. In the absence of any heating, the cooling of planetary mantles following the solidification of a magma ocean would cause the lithospheric thickness to increase with time t as $\sqrt{\kappa t}$, where κ is the thermal diffusivity and T_e would be >100 km by $t \sim 500$ Myr (Watts et al., 2013). However, tidal heating and radiogenic heating could significantly slow down the early Moon's cooling and even prolong the magma ocean for >100 Myr to explain the lunar crustal ages (Elkins-Tanton et al., 2011; Meyer et al., 2010), hindering lithospheric thickening.

Thickness of elastic lithosphere, T_e, can be determined by using observed gravity and topography anomalies of geological features and can help inform us about mantle viscosity structure (e.g., Zhong & Watts, 2013). The mare basalts were formed at ~3.7–3.9 Ga, enabling estimates of T_e for that time period. The inferred T_e is on average ~50 km for the lunar basins, but significant spatial variabilities in T_e exist (Arkani-Hamed, 1998; Audet & Johnson, 2011; Solomon & Head, 1980; Sugano & Heki, 2004; Wieczorek et al., 2006). In our model, time $t = 0$ is when the lithosphere starts to form and grow, following solidification of the magma ocean ~100 Myr after lunar accretion (Elkins-Tanton et al., 2011; Meyer et al., 2010). Our model does not include the magma ocean era, which with negligibly small T_e does not support the fossil bulges. In our model, $T_e = 0$ at $t = 0$ and $T_e = 50$ km at mare basalt formation time (i.e., our model time $t = 500$ Myr or 3.9 Ga) serve as two anchor points. In our reference model, T_e increases from 0 at $t = 0$ to 50 km at $t = 500$ Myr as $\sqrt{t}$ and then to 150 km at $t = 4.4$ Gyr at present (Figure 1c). At any given time, the viscosity for elastic lithosphere is set sufficiently high (i.e., 10^{30} Pa s) to maintain elastic behavior, and the viscosity below the lithosphere decreases to mantle background viscosity of $\eta_0 = 10^{22}$ Pa s over the thickness of 2 T_e (Figure 1d). This time-dependent

model for lunar lithosphere and viscosity undoubtedly has quite some uncertainties. We have performed sensitivity studies to examine the robustness of our results. As to be demonstrated later, our results are mainly sensitive to T_e evolution before the bulge formation is completed (i.e., for $t < 400$ Myr for all the relevant cases considered in this study) but are independent of mantle viscosity and T_e evolution once the bulge is produced (provided that T_e does not decrease with time).

2.3. Applied Potential From Rotational and Tidal Effects and Its Time Dependence

The tidal-rotational forcing depends on lunar rotational rate and orbital state. Theoretical studies of lunar orbital and rotational evolutions suggest that the Moon may have experienced periods of nonzero eccentricity, nonsynchronous spin, and higher obliquity (i.e., the Cassini state transition) (e.g., Garrick-Bethell et al., 2006; Siegler et al., 2011). Although their timings are largely unknown, these orbital and rotational states may have had implications for the lunar fossil bulge (Garrick-Bethell et al., 2006; Keane & Matsuyama, 2014; Matsuyama, 2013). However, Meyer et al. (2010) propose that the lunar bulge cannot be possibly formed with large orbital eccentricity because of the resulting large elastic deformation, suggesting that the bulge may have been formed after lunar orbital state is largely stabilized. Here we assume that the Moon is on a circular, tidally locked synchronous orbit relative to the Earth at any time. The resulting spherical harmonic degree 2 tidal potential is (Wahr et al., 2009)

$$V_t = \frac{3GM_E r^2}{2a^3}\left[\frac{1}{6}\left(1 - 3\cos^2\theta\right) + \frac{1}{2}\sin^2\theta\cos2\phi\right], \tag{5}$$

where M_E is the mass of the Earth, a is the lunar orbital semimajor axis, and r, θ, and ϕ are the radial, colatitudinal, and longitudinal coordinates on the Moon. The rotational potential is

$$V_r = \frac{1}{6}\Omega^2 r^2\left(1 - 3\cos^2\theta\right), \tag{6}$$

where Ω is the lunar rotation rate. The synchronous rotation of the Moon on a circular orbit leads to $GM_E/a^3 = \Omega^2$ (i.e., Kepler's third law). The total potential can be written in terms of the Legendre functions $P_l^m(\cos\theta)$ of degree and order $(l,m) = (2,0)$ and $(2,2)$, as

$$V = V_t + V_r = \Omega^2 r^2\left[-\frac{5}{6}P_2^0(\cos\theta) + \frac{1}{4}P_2^2(\cos\theta)\cos2\phi\right]. \tag{7}$$

With the applied potential in equation (7), the hydrostatic theory for a "fluid" planet (i.e., the entire planet behaves like a fluid with no elastic lithosphere to support long-term stress) would suggest that the ratio of the (2,0) to (2,2) gravitational coefficients, C_{20}/C_{22}, is $-10/3$.

In our modeling, without loss of generality we only consider (2,0) potential in equation (7) as the applied potential V, which can be written in spherical harmonic function $Y_{20}(\theta, \phi)$ as

$$V = -\frac{5}{6}\Omega^2 r^2 P_2^0(\cos\theta) = -\frac{\sqrt{5\pi}}{3}\Omega^2 r^2 Y_{20}(\theta, \phi). \tag{8}$$

This is entirely justified, because the displacement and gravitational responses (i.e., Love numbers) to (2,0) and (2,2) applied potentials are identical and independent from each other, for a depth-dependent viscoelastic structure.

The applied potential decreases monotonically with time as the Moon's rotation rate Ω decreases on a tidally locked synchronous orbit that recedes from the Earth (i.e., semimajor axis a increases), due to the Earth's tidal dissipation (Figure 1a). We employ a simple but commonly used orbital evolution model by Murray and Dermott (1999) to calculate the semimajor axis $a(t)$ through an integral form of the equation

$$a(t)^{\frac{13}{2}} = a(t_0)^{\frac{13}{2}} + \frac{13}{2}\frac{k_2}{Q}A(t - t_0), \tag{9}$$

where t_0 is a starting time (not necessarily $t = 0$), Q is the average tidal dissipation factor in the period from t_0 to t, k_2 is the Earth's tidal Love number, $A = \frac{3mR_E^5}{M_E}[G(M_E + m)]^{\frac{1}{2}}$ is a constant with m, M_E, and R_E as Moon's mass, Earth's mass, and radius, respectively. Following Lambeck and Pullan (1980), the Earth's tidal Love number k_2 is taken as a fixed value of 0.3 in our model. This is justified for two reasons. First, k_2 is determined by the Earth's elastic parameters that are insensitive to temperature. For example, shear modulus changes by
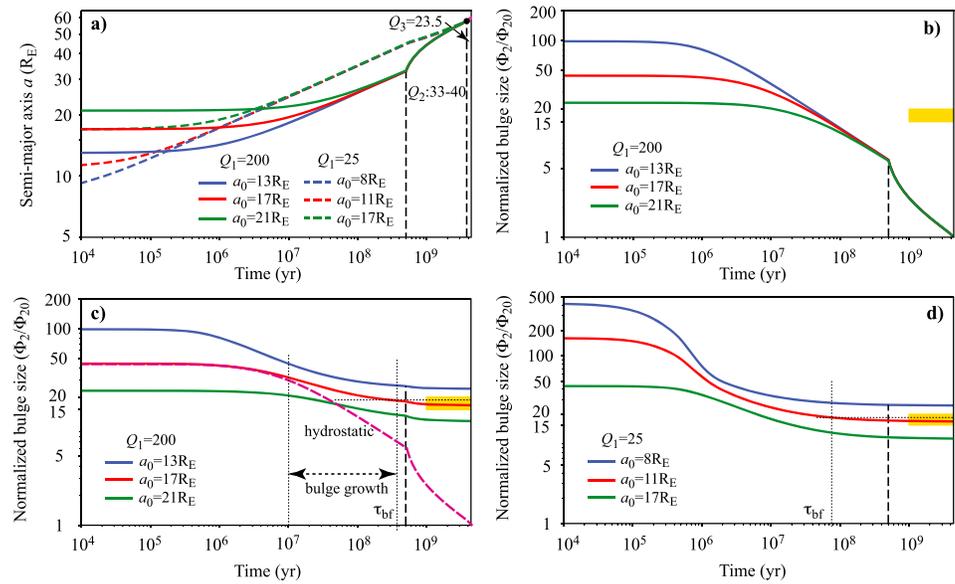
Figure 2. Time evolution of semimajor axis a of lunar orbit and lunar bulge sizes. (a) Time evolution of a for different values of Q and a_0 (Murray & Dermott, 1999). a can be converted to the applied potential that drives the deformation. (b) Time evolution of model bulge size that is normalized by the present-day hydrostatic value for models with no lithosphere (i.e., fluid) and $Q_1 = 200$ and three different a_0. (c) The same as in Figure 2b except for including the thickening lithosphere in Figure 1c. The dashed curve is the same as that in Figure 2b with $a_0 = 17 R_E$. (d) The same as in Figure 2c but for $Q_1 = 25$ and three different a_0. In Figures 2b–2d, the yellow bar marks the range of observed normalized bulge size (i.e., 15 to 20). The thin vertical dashed line in Figures 2c and 2d marks the bulge formation time τ_{bf}.

<10% for ~500 K variations in temperature (e.g., Anderson, 1989). Second, after the relatively rapid solidification of the mantle magma ocean (e.g., Carlson et al., 2014), the Earth's mantle may only cool by <500 K throughout its geological history (e.g., Herzberg et al., 2010). Therefore, our lunar orbital evolution model for semimajor axis a (i.e., equation (9)) and hence the applied tidal-rotational potential (Figure 1a) has two controlling parameters: initial semimajor axis at $t = 0$, a_0, and Earth's tidal dissipation Q value. A larger Q value implies less tidal dissipation in the Earth and slower lunar recession from the Earth. Since the recession rate $\dot{a} \propto a^{-\frac{11}{2}}$, a increases significantly faster at earlier time stages (Figure 2a). Note that the orbital evolution in equation (9) depends on ratio k_2/Q which is used in some studies (e.g., Bills & Ray, 1999) as the controlling parameter.

Earth's tidal Q value may vary significantly in the past (Bills & Ray, 1999). The present-day Q value is largely controlled by tidal dissipation in the Earth's oceans (Egbert & Ray, 2000; Munk, 1997) and is responsible for ~3.8 cm/yr lunar recession rate as observed from the lunar laser ranging (Dickey et al., 1994). Although the Q value is ~12 as constrained by the lunar laser ranging data (e.g., Bills & Ray, 1999) using $k_2 = 0.3$, it must be significantly larger in the past to prevent a from collapsing to zero at 1.5 Ga (e.g., Bills & Ray, 1999; Lambeck & Pullan, 1980). Using lunar orbital evolution model of Webb (1982), Bills and Ray (1999) showed that k_2/Q between 1 and 3 Ga is ~30% of the present day's, corresponding to $Q \sim 40$. Lambeck and Pullan (1980) used $Q \sim 30$ in their lunar orbital model. However, observational constraints on long-term lunar orbital evolution come from sedimentary records of tidal rhythmites that suggest that a increases from 58 R_E at ~620 Ma to the current 60 R_E but is less constrained in early times (Williams, 2000). Using equation (9), the observations suggest that Q is 23.5 for the last 620 Ma.

Our lunar orbital evolution history is divided into three stages defined by different Q values. The third stage is for the most recent time period from 620 Ma to the present day with $Q = 23.5$ (i.e., Q_3). The first stage (Q_1) covers the first 500 Myr of our model (i.e., from 4.4 to 3.9 Ga) and employs a variable Q value from 25 to 500. Note that the present-day mantle Q is ~400–500 at tidal frequencies (Anderson & Given, 1982) which can be viewed as an upper bound on Q_1. Also, the ending time of the first stage at 3.9 Ga corresponds approximately to the Hadean-Archean boundary. For given a_0, Q_1, and Q_3, Q for the second stage, Q_2, is determined by bridging a between the first and third stages (Figure 2a). Q_2 is found to range from 33 to 40 for our

models. Orbital evolution models with more time stages are possible but may not be justified by available constraints. Note that the evolution of a is mainly controlled by Q_1, while the effect of a_0 is secondary. For example, for $Q_1 = 25$ but three different values of a_0, a becomes nearly the same at $t \sim 5$ Myr and is ~43 R_E at $t = 500$ Myr (Figure 2a). However, for $Q_1 = 200$, a evolves much slowly and is ~32 R_E at $t = 500$ Myr for different a_0. The semimajor axis is converted to the rotation rate and applied potential V in equation (8), using the relation $\Omega^2 = GM_E/a^3$.

2.4. Computational Method

For this study, we develop an efficient semianalytical, propagator matrix based method to solve the governing equations (1)–(3) with time-dependent viscoelastic rheology (4) and applied potential (8) for long-term bulge development of the Moon. In this method, equations (1)–(4) are discretized and solved directly in the time domain, and in each time step the spatial dependence of any variable is expressed as a spherical harmonic function (i.e., $Y_{20}(\theta, \phi)$) in lateral directions and as discrete layers in the radial direction. The theoretical derivation of the method, method validation, and model time and radial resolution are given in the supporting information (Text S1 and Figure S3).

3. Results

We compute the size of lunar bulge as function of time for different orbital evolution histories (e.g., Figure 2a) with model variables a_0 and Q_1. We measure the model lunar bulge by computing ratio Φ_2/Φ_{20} (referred to as normalized bulge size hereafter), where Φ_2 is the time-dependent degree 2 zonal gravitational potential anomaly from our model and Φ_{20} is the present-day hydrostatic counterpart (Figures 2b–2d). Since the observed present-day Φ_2/Φ_{20} after basin correction is ~17 (Keane & Matsuyama, 2014), a scenario is taken as "successful" if the modeled present-day normalized bulge size falls within a range of 15 to 20 (Figures 2b–2d). It is worth noting here that the basin-corrected gravitational potential anomalies by Keane and Matsuyama (2014) did not account for possible contribution from degree 2 crustal thickness variations that tidal heating may have caused (Garrick-Bethell et al., 2014). However, based on crustal compensation calculations using degree 2 basin-corrected topography from Garrick-Bethell et al. (2014), we suggest that such an effect may modify the corrected Φ_2/Φ_{20} by no more than 15% (Text S2), supporting our model and interpretation that the basin-corrected degree 2 gravity anomalies are mainly caused by the fossil bulge.

We first computed a fluid model with $Q_1 = 200$ (Figure 2a) and a viscosity of 10^{22} Pa s everywhere (i.e., no lithosphere). In this model, the Moon would behave like a fluid planet and cannot support deviatoric stress over several Maxwell times (i.e., $\sim10^5$ years). The model bulge sizes decrease with time as a increases (Figure 2b) or the applied potential decreases. As expected, the normalized bulge size is 1 at the present day for the fluid models, significantly smaller than the observed values that we take as ranging from 15 to 20 here. Note that the bulge sizes for the fluid models agree with the hydrostatic value at any given time.

The decrease in the applied potential with time is equivalent to applying a pressure load to the surface. This load would be fully compensated by surface displacement or topography when no lithosphere is present (e.g., Figure 2b). However, the lithosphere may partially support this load, causing lithospheric stress and reduced surface topography (i.e., the fossil bulge). In our model with thickening lithosphere, for the first ~10 Myr when the lithosphere is still thin, the bulge size is similar to the fluid model (Figure 2c). However, as the lithosphere thickens and starts to support stresses (Figure 3), the bulge does not reduce as much compared with the fluid model and remains unchanged after several hundred million years (Figure 2c). For the case with $Q_1 = 200$ and $a_0 = 17$ R_E, the present-day bulge size is well within the observed range (Figure 2c). For this case, the lithospheric stress reaches a maximum of ~25 MPa at depths <30 km after several hundred million years, and the stress field remains largely unchanged afterward (Figures 3a–3d). Given that lithospheric strength exceeds 100 MPa (Kohlstedt & Mackwell, 2009), the lithosphere should be able to maintain the bulges with lithospheric stress.

We have computed a large number of cases with Q_1 from 25 to 500 and a_0 from 5 R_E to 25 R_E. The results show that for a given Q_1, there is a limited range of a_0 (~3 R_E) that can reproduce the observed bulges, and too small (large) of an a_0 overpredicts (underpredicts) the observed bulge size (Figure 4a). Also, a smaller Q_1 needs to be compensated by a smaller a_0 to reproduce the observed bulges (Figure 4a). For example, for $Q_1 = 25$, the observed bulge is obtained for $a_0 \sim 11$ R_E (Figure 2d), much smaller than $a_0 \sim 17$ R_E for
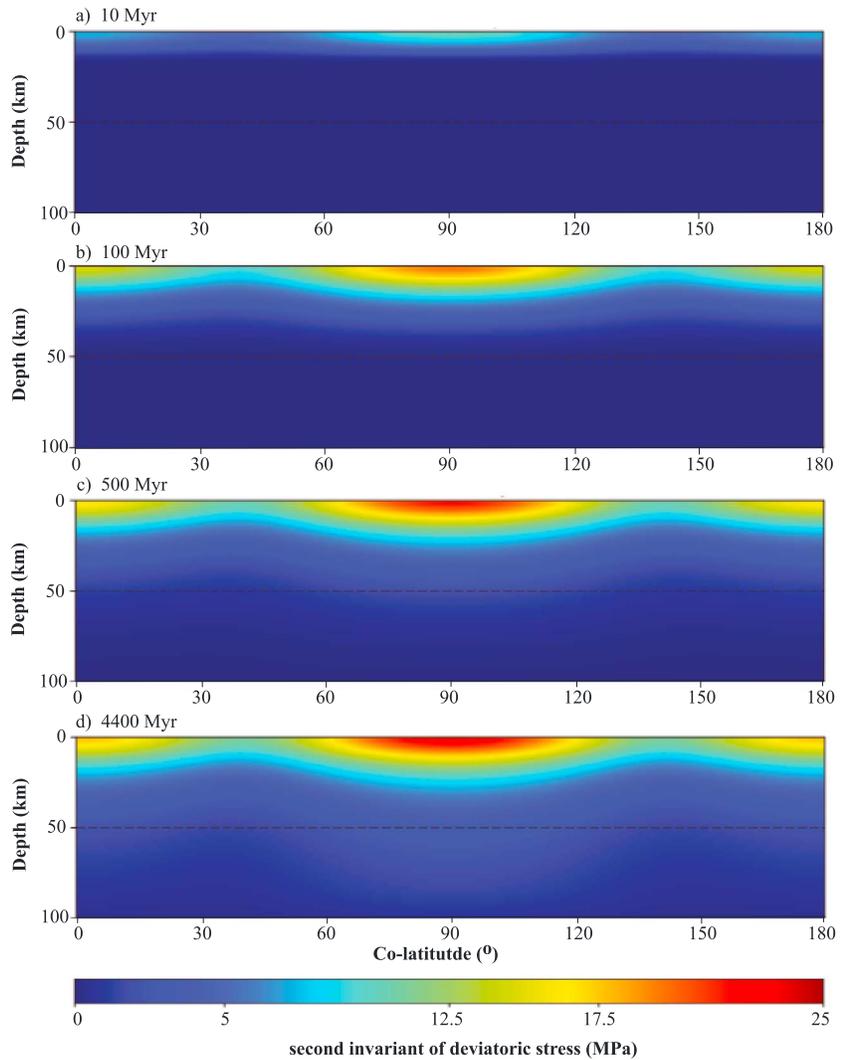
Figure 3. Spatial and temporal distribution of second invariant of deviatoric stress for the reference model with $Q_1 = 200$ and $a_0 = 17\ R_E$. The stress at different colatitude (from 0 to 180°) for the top 100 km of the Moon at (a) 10 Myr, (b) 100 Myr, (c) 500 Myr, and (d) 4.4 Gyr (or present day). Note that the stress is concentrated at shallow depths and remains largely unchanged after the bulges are formed.

$Q_1 = 200$. This is because for smaller Q_1 but a fixed a_0, a increases more rapidly in the early time period (Figure 2a) during which the elastic lithosphere is thinner and maintains a smaller bulge (Figures 2c and 2d).

The bulge formation is a continuous process that occurs over some time period (e.g., Figure 2c). However, for models that reproduce the observed bulges, we may define a bulge formation time, τ_{bf}, marking the time when the bulge size falls within a factor of 1.1 of the present-day value (i.e., when the bulge is largely stabilized). For example, for $Q_1 = 200$ and $a_0 = 17\ R_E$, $\tau_{bf} \cong 380$ Myr, while for $Q_1 = 25$ and $a_0 = 11\ R_E$, $\tau_{bf} \cong 80$ Myr (Figures 2c and 2d). Accordingly, the semimajor axis a_{bf} can be found from the orbital evolution (e.g., Figure 2a) to be 31.5 R_E and 34 R_E, respectively, for these two cases. For all the cases that reproduce the observed bulges, while τ_{bf} ranges from 70 to 550 Myr, a_{bf} is in a tighter range of 30 R_E to 34 R_E (Figure 4b). A larger Q_1 corresponds to slower bulge formation (Figures 2c and 2d).

The inferred T_e of 50 km at mare basalt formation time may vary spatially with considerable uncertainty (Arkani-Hamed, 1998; Audet & Johnson, 2011; Solomon & Head, 1980; Sugano & Heki, 2004; Wieczorek et al., 2006). We found that varying T_e between 30 km and 80 km at $t = 500$ Myr leads to ~ ± 20% change in the present-day bulge size (Figure S1a). Such changes can be compensated by varying a_0 by <~1.5 R_E
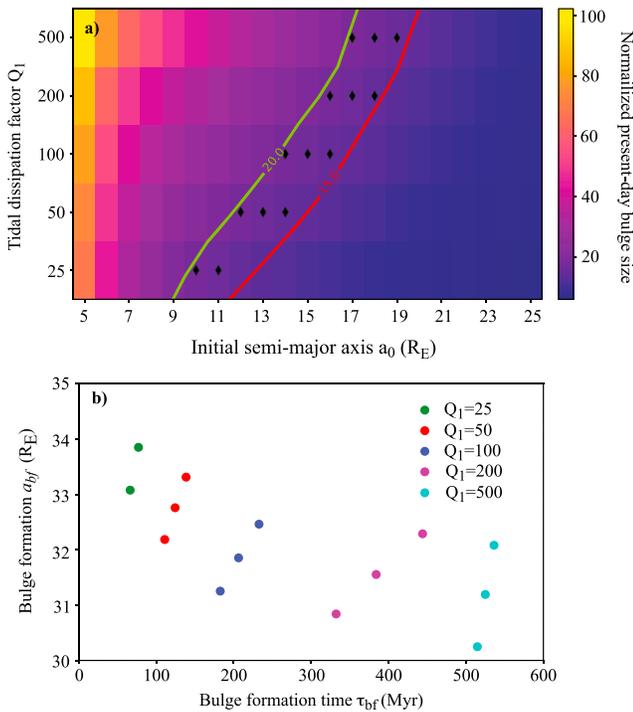
Figure 4. Dependence and characteristics of the model bulge size. (a) Dependence of the normalized present-day bulge size on Q_1 and a_0 for the reference rheological model. The black diamonds mark the cases that reproduce the range of observed bulge size, and the red and green curves are isocontours for bulge size of 15 and 20, respectively. (b) Bulge formation time τ_{bf} and semimajor axis a_{bf} for all the models that reproduce the observed bulges.

for a given Q_1 (Figure 4a), suggesting the robustness of our results. We also found that the bulge evolution is insensitive to how T_e increases with time after the bulge formation and to mantle interior viscosity. For example, the bulge evolution for cases in which T_e is kept at 50 km after 500 Myr is nearly the same as that for the corresponding cases with the lithospheric thickening with time after 500 Myr (Figure S1b). Reducing mantle interior viscosity from 10^{22} to 10^{21} Pa s does not change the results either (Figure S1c).

4. Conclusion and Discussion

We have formulated the first dynamic model for lunar fossil bulges. Using a propagator matrix based, semianalytical method for computing viscoelastic deformation, the model determines bulge formation for the Moon with lithospheric thickening and time-decreasing tidal-rotational forcing due to the lunar recession from the Earth. We demonstrate that the observed lunar bulges may have been produced in the first 100 Myr to 500 Myr following the formation of lunar lithosphere, depending on tidal Q value of the Hadean Earth (i.e., Q_1 in Figure 4). However, we suggest that the lunar bulges were produced relatively slowly with Q_1 considerably larger than the Q value ($Q_3 = 23.5$) for the last 620 Myr. For $Q_1 \sim 25$, the bulges would have formed rapidly before the lithosphere thickened significantly (Figure 2d), and the lithospheric stress would have been confined to <5 km depths with a maximum value of 75 MPa (Figure S2). The lunar crust is heavily fractured in general to depths of 5–10 km, as interpreted from crustal porosity models derived from Gravity Recovery and Interior Laboratory gravity data (Besserer et al., 2014). The bulge stresses would likely have been relieved by the shock pressures of sufficiently large impacts, but we can also state that the frictional strength of lithosphere is <75 MPa over an ~ 5 km depth interval (Byerlee, 1978). However, if the bulges formed slowly with $Q_1 \sim 200$–300, then there would have been smaller bulge stresses extending to greater depths (Figure 3), and these stresses would likely have been supported by the lunar lithosphere over the Moon's geological history.

The slow bulge formation with large Q_1 corresponds to slow recession rate for the early Moon. For example, the mean recession rate is ~ 0.08 R_E/Myr for the first 100 Myr of the model with $Q_1 = 200$ and $a_0 = 17$ R_E, and by contrast it is ~ 0.24 R_E/Myr for the same period for $Q_1 = 25$ and $a_0 = 11$ R_E (Figure 2a). Although the early lunar orbit evolution is likely more complicated (e.g., Meyer et al., 2010; Siegler et al., 2011), considering that the Moon might have receded from several Earth radii where it was likely formed to a_0 over the magma ocean era, the models with $Q_1 \sim 200$–300 are more compatible with ~ 0.1 R_E/Myr recession rate over the ~ 100 Myr lifetime of the magma ocean (Elkins-Tanton et al., 2011).

Therefore, we conclude that the lunar bulges had been formed by ~ 4 Ga (i.e., $t \sim 400$ Myr in Figures 2c and 4b) when $a \sim 32$ R_E and the Earth had a relatively large Q_1 value of ~ 200–300. We want to make four remarks on this conclusion. (1) Our proposed large Q for the early Earth is consistent with studies of lunar obliquity (Chen & Nimmo, 2016) and orbital history (Bills & Ray, 1999; Lambeck & Pullan, 1980). (2) Although our formulation for fossil bulge formation differs significantly from previous studies, it is interesting to note that our conclusion of $a \sim 32$ R_E when the bulge formation is completed is consistent with Garrick-Bethell et al. (2014) but larger than those from Lambeck and Pullan (1980) and Matsuyama (2013). (3) We reiterate that our results on Q are obtained with $k_2 = 0.3$ (i.e., elastic tidal Love number) (e.g., Lambeck & Pullan, 1980), although the orbital evolution depends on ratio k_2/Q (equation (9)). If a fluid Love number $k_2 \sim 0.96$ is used as in Chen and Nimmo (2016), our results would remain the same, except that all the Q values would have to be increased by a factor of 3.2. (4) Although different time epochs may be considered in future studies, we do not think that our conclusion is biased by the choice of 500 Myr for the first epoch, because the bulge formation time differs significantly among models with different Q_1 and is mostly much less than 500 Myr (Figure 4b).

The present-day Earth's tidal dissipation occurs predominantly in oceans, both at shallow seas and deep open ocean (e.g., Egbert & Ray, 2000), leading to relatively small Q (e.g., Bills & Ray, 1999). The significantly larger Q (~200–300) for the early Earth before 4 Ga (or the Hadean) inferred from our study, compared with that for the last 4 Gyr (i.e., $Q_2 \sim 35$ from 4 Ga to 620 Ma and $Q_3 \sim 25$ for the last 620 Myr), suggests that the Hadean Earth might have a very different surface environment from that of today and the last 4 Gyr. Continental area in the Hadean was probably significantly smaller than that since the Phanerozoic (Stein & Ben-Avraham, 2015), and if the Hadean Earth had a deep ocean and smooth ocean floor, then the absence of shallow seas would reduce tidal dissipation. However, depending on seafloor roughness, dissipation in the deep ocean by itself may be significant enough to result in a too small Q to account for the slow lunar recession required by the lunar bulge formation.

A more plausible inference from our model is that the Hadean hydrosphere, if existent, may have been frozen to depth in a "snowball" state. A frozen snowball state is geologically evident for various periods in the Proterozoic (Hoffman et al., 1998; Kirschvink, 1992; Macdonald et al., 2010) and would be consistent with the findings that the oldest sedimentary rocks are younger than 4 Ga (Moorbath et al., 1973; Nutman et al., 1997; Tashiro et al., 2017). A snowball Earth at Hadean time before 4 Ga is likely as a consequence of the fainter early Sun that emitted ~30% less energy than today (Bahcall et al., 2001; Ringwood, 1961). High concentration of greenhouse gases including CO_2 or methane or both is considered crucial to counter the effect of the faint early Sun as to produce oceans in the Archean (Feulner, 2012; Sagan & Chyba, 1997). Therefore, an important question is how and when the greenhouse gases are accumulated to a sufficient level to thaw a frozen hydrosphere from the Hadean to Archean Earth (Feulner, 2012; Marchi et al., 2016). Although direct evidence for a snowball Hadean Earth is lacking, the mechanism for escaping the snowball state is still debated (Feulner, 2012), and Q's dependence on ice water fraction for a snowball Earth (e.g., Wunsch, 2016) and on continental configuration (e.g., Lambeck & Pullan) is uncertain; our lunar fossil bulge formation model provides new and unique insights into studies of climate and surface environment of the early Earth.

References

Anderson, D. L. (1989). *Theory of the Earth*. Boston: Blackwell Scientific.

Anderson, D. L., & Given, J. W. (1982). Absorption band Q model for the Earth. *Journal of Geophysical Research*, 87, 3893–3904. https://doi.org/10.1029/JB087iB05p03893

Arkani-Hamed, J. (1998). The lunar mascons revisited. *Journal of Geophysical Research*, 103, 3709–3739. https://doi.org/10.1029/97JE02815

Audet, P., & Johnson, C. L. (2011). Lithospheric structure of the Moon and correlation with deep moonquake source regions. In *Lunar and Planetary Science Conference* (Vol. 42, 1742 pp.).

Bahcall, J. N., Pinsonneault, M. H., & Basu, S. (2001). Solar models: Current epoch and time dependences, neutrinos, and helioseismological properties. *The Astrophysical Journal*, 555(2), 990–1012. https://doi.org/10.1086/321493

Besserer, J., Nimmo, F., Wieczorek, M. A., Weber, R. C., Kiefer, W. S., McGovern, P. J., … Zuber, M. T. (2014). GRAIL gravity constraints on the vertical and lateral density structure of the lunar crust. *Geophysical Research Letters*, 41, 5771–5777. https://doi.org/10.1002/2014GL060240

Bills, B. G., & Ray, R. D. (1999). Lunar orbital evolution: A synthesis of recent results. *Geophysical Research Letters*, 26, 3045–3048. https://doi.org/10.1029/1999GL008348

Byerlee, J. (1978). Friction of rocks. *Pure and applied geophysics*, 116(4-5), 615–626. https://doi.org/10.1007/BF00876528

Carlson, R. W., Borg, L. E., Gaffney, A. M., & Boyet, M. (2014). Rb-Sr, Sm-Nd and Lu-Hf isotope systematics of the lunar Mg-suite: the age of the lunar crust and its relation to the time of Moon formation. *Philosophical Transactions of the Royal Society A*, 372(2024), 20130246. https://doi.org/10.1098/rsta.2013.0246

Chen, E. M., & Nimmo, F. (2016). Tidal dissipation in the lunar magma ocean and its effect on the early evolution of the Earth–Moon system. *Icarus*, 275, 132–142. https://doi.org/10.1016/j.icarus.2016.04.012

Dickey, J. O., Bender, P. L., Faller, J. E., Newhall, X. X., Ricklefs, R. L., Ries, J. G., … Williams, J. G. (1994). Lunar laser ranging: A continuing legacy of the Apollo program. *Science*, 265(5171), 482–490. https://doi.org/10.1126/science.265.5171.482

Egbert, G. D., & Ray, R. D. (2000). Significant dissipation of tidal energy in the deep ocean inferred from satellite altimeter data. *Nature*, 405(6788), 775–778. https://doi.org/10.1038/35015531

Elkins-Tanton, L. T., Burgess, S., & Yin, Q. Z. (2011). The lunar magma ocean: Reconciling the solidification process with lunar petrology and geochronology. *Earth and Planetary Science Letters*, 304, 326–336. https://doi.org/10.1016/j.epsl.2011.02.004

Feulner, G. (2012). The faint young Sun problem. *Reviews of Geophysics*, 50, RG2006. https://doi.org/10.1029/2011RG000375

Garrick-Bethell, I., Perera, V., Nimmo, F., & Zuber, M. T. (2014). The tidal-rotational shape of the Moon and evidence for polar wander. *Nature*, 512(7513), 181–184. https://doi.org/10.1038/nature13639

Garrick-Bethell, I., Wisdom, J., & Zuber, M. T. (2006). Evidence for a past high-eccentricity lunar orbit. *Science*, 313, 652–655. https://doi.org/10.1126/science.1128237

Hager, B. H., & O'Connell, R. J. (1981). A simple global model of plate dynamics and mantle convection. *Journal of Geophysical Research*, 86, 4843–4867. https://doi.org/10.1029/JB086iB06p04843

Hanyk, L., Yuen, D. A., & Matyska, C. (1996). Initial-value and modal approaches for transient viscoelastic responses with complex viscosity profiles. *Geophysical Journal International*, 127(2), 348–362. https://doi.org/10.1111/j.1365-246X.1996.tb04725.x

Herzberg, C., Condie, K., & Korenaga, J. (2010). Thermal history of the Earth and its petrological expression. *Earth and Planetary Science Letters*, 292, 79–88. https://doi.org/10.1016/j.epsl.2010.01.022

Hoffman, P. F., Kaufman, A. J., Halverson, G. P., & Schrag, D. P. (1998). A Neoproterozoic snowball Earth. *Science*, *281*(5381), 1342–1346. https://doi.org/10.1126/science.281.5381.1342

Jeffreys, H. (1915). Certain hypotheses as to the internal structure of the Earth and Moon. *Memoirs of the Royal Astronomical Society*, *60*, 187.

Kamata, S., Sugita, S., & Abe, Y. (2012). A new spectral calculation scheme for long-term deformation of Maxwellian planetary bodies. *Journal of Geophysical Research*, *117*, E02004. https://doi.org/10.1029/2011JE003945

Keane, J. T., & Matsuyama, I. (2014). Evidence for lunar true polar wander and a past low-eccentricity, synchronous lunar orbit. *Geophysical Research Letters*, *41*, 6610–6619. https://doi.org/10.1002/2014GL061195

Kirschvink, J. L. (1992). Late Proterozoic low-latitude global glaciation: The snowball Earth. In J. W. Schopf, & C. Klein (Eds.), *The Proterozoic Biosphere: A Multidisciplinary Study* (pp. 51–52). New York: Cambridge University Press.

Kohlstedt, D. L., & Mackwell, S. J. (2009). Strength and deformation of planetary lithospheres. In T. Waters, & R. Schultz (Eds.), *Planetary Tectonics*, (pp. 395–455). New York: Cambridge University Press. https://doi.org/10.1017/CBO9780511691645.010

Lambeck, K., & Pullan, S. (1980). The lunar fossil bulge hypothesis revisited. *Physics of the Earth and Planetary Interiors*, *22*(1), 29–35. https://doi.org/10.1016/0031-9201(80)90097-7

Laplace, P. S. (1798). *Traité de MéCanique CéLeste* (Vol. 2). Paris Duprat: Bachlier.

Macdonald, F. A., Schmitz, M. D., Crowley, J. L., Roots, C. F., Jones, D. S., Maloof, A. C., … Schrag, D. P. (2010). Calibrating the cryogenian. *Science*, *327*, 1241–1243. https://doi.org/10.1126/science.1183325

Marchi, S., Black, B. A., Elkins-Tanton, L. T., & Bottke, W. F. (2016). Massive impact-induced release of carbon and sulfur gases in the early Earth's atmosphere. *Earth and Planetary Science Letters*, *449*, 96–104. https://doi.org/10.1016/j.epsl.2016.05.032

Matsuyama, I. (2013). Fossil figure contribution to the lunar figure. *Icarus*, *222*(1), 411–414. https://doi.org/10.1016/j.icarus.2012.10.025

Melosh, H. J., Freed, A. M., Johnson, B. C., Blair, D. M., Andrews-Hanna, J. C., Neumann, G. A., … Zuber, M. T. (2013). The origin of lunar mascon basins. *Science*, *340*(6140), 1552–1555. https://doi.org/10.1126/science.1235768

Meyer, J., Elkins-Tanton, L., & Wisdom, J. (2010). Coupled thermal–orbital evolution of the early Moon. *Icarus*, *208*, 1–10. https://doi.org/10.1016/j.icarus.2010.01.029

Moorbath, S., O'nions, R. K., & Pankhurst, R. J. (1973). Early Archaean age for the Isua iron formation, West Greenland. *Nature*, *245*(5421), 138–139. https://doi.org/10.1038/245138a0

Munk, W. (1997). Once again: Once again—Tidal friction. *Progress in Oceanography*, *40*(1-4), 7–35. https://doi.org/10.1016/S0079-6611(97)00021-9

Murray, C. D., & Dermott, S. F. (1999). *Solar System Dynamics*. Cambridge, UK: Cambridge University Press.

Nutman, A. P., Mojzsis, S. J., & Friend, C. R. (1997). Recognition of ≥ 3850 Ma water-lain sediments in West Greenland and their significance for the early Archaean Earth. *Geochimica et Cosmochimica Acta*, *61*(12), 2475–2484. https://doi.org/10.1016/S0016-7037(97)00097-5

Qin, C., Zhong, S., & Wahr, J. (2014). A perturbation method and its application: Elastic tidal response of a laterally heterogeneous planet. *Geophysical Journal International*, *199*(2), 631–647. https://doi.org/10.1093/gji/ggu279

Ringwood, A. E. (1961). Changes in solar luminosity and some possible terrestrial consequences. *Geochimica et Cosmochimica Acta*, *21*(3-4), 295–296. https://doi.org/10.1016/S0016-7037(61)80064-1

Robuchon, G., Choblet, G., Tobie, G., Čadek, O., Sotin, C., & Grasset, O. (2010). Coupling of thermal evolution and despinning of early Iapetus. *Icarus*, *207*, 959–971. https://doi.org/10.1016/j.icarus.2009.12.002

Sagan, C., & Chyba, C. (1997). The early faint Sun paradox: Organic shielding of ultraviolet-labile greenhouse gases. *Science*, *276*(5316), 1217–1221. https://doi.org/10.1126/science.276.5316.1217

Sedgwick, W. F. (1898). On the figure of the Moon. *Messenger Math*, *27*, 171–173.

Siegler, M. A., Bills, B. G., & Paige, D. A. (2011). Effects of orbital evolution on lunar ice stability. *Journal of Geophysical Research*, *116*, E03010. https://doi.org/10.1029/2010JE003652

Solomon, S. C., & Head, J. W. (1980). Lunar mascon basins: Lava filling, tectonics, and evolution of the lithosphere. *Reviews of Geophysics*, *18*, 107–141. https://doi.org/10.1029/RG018i001p00107

Stein, M., & Ben-Avraham, Z. (2015). Mechanism of continental crust growth. In *Treatise on Geophysics* (2nd ed., Vol. 9, pp. 173–199).

Sugano, T., & Heki, K. (2004). Isostasy of the Moon from high-resolution gravity and topography data: Implication for its thermal history. *Geophysical Research Letters*, *31*, L24703. https://doi.org/10.1029/2004GL022059

Tashiro, T., Ishida, A., Hori, M., Igisu, M., Koike, M., Méjean, P., … Komiya, T. (2017). Early trace of life from 3.95 Ga sedimentary rocks in Labrador, Canada. *Nature*, *549*(7673), 516. https://doi.org/10.1038/nature24019

Tobie, G., Čadek, O., & Sotin, C. (2008). Solid tidal friction above a liquid water reservoir as the origin of the south pole hotspot on Enceladus. *Icarus*, *196*, 642–652. https://doi.org/10.1016/j.icarus.2008.03.008

Tromp, J., & Mitrovica, J. X. (1999). Surface loading of a viscoelastic Earth—II. Spherical models. *Geophysical Journal International*, *137*, 856–872. https://doi.org/10.1046/j.1365-246x.1999.00839.x

Wahr, J., Selvans, Z. A., Mullen, M. E., Barr, A. C., Collins, G. C., Selvans, M. M., & Pappalardo, R. T. (2009). Modeling stresses on satellites due to nonsynchronous rotation and orbital eccentricity using gravitational potential theory. *Icarus*, *200*, 188–206. https://doi.org/10.1016/j.icarus.2008.11.002

Watts, A. B., Zhong, S. J., & Hunter, J. (2013). The behavior of the lithosphere on seismic to geologic timescales. *Annual Review of Earth and Planetary Sciences*, *41*(1), 443–468. https://doi.org/10.1146/annurev-earth-042711-105457

Webb, D. J. (1982). Tides and the evolution of the Earth—Moon system. *Geophysical Journal International*, *70*(1), 261–271. https://doi.org/10.1111/j.1365-246X.1982.tb06404.x

Weber, R. C., Lin, P. Y., Garnero, E. J., Williams, Q., & Lognonne, P. (2011). Seismic detection of the lunar core. *Science*, *331*, 309–312. https://doi.org/10.1126/science.1199375

Wieczorek, M. A. (2007). Gravity and topography of the terrestrial planets. *Treatise on Geophysics*, *10*, 165–206. https://doi.org/10.1016/B978-044452748-6/00156-5

Wieczorek, M. A., Jolliff, B. L., Khan, A., Pritchard, M. E., Weiss, B. P., Williams, J. G., … McCallum, I. S. (2006). The constitution and structure of the lunar interior. *Reviews in Mineralogy and Geochemistry*, *60*, 221–364. https://doi.org/10.2138/rmg.2006.60.3

Williams, G. E. (2000). Geological constraints on the Precambrian history of Earth's rotation and the Moon's orbit. *Reviews of Geophysics*, *38*, 37–59. https://doi.org/10.1029/1999RG900016

Wunsch, C. (2016). Tides of global ice-covered oceans. *Icarus*, *274*, 122–130. https://doi.org/10.1016/j.icarus.2016.03.026

Zhong, S., Paulson, A., & Wahr, J. (2003). Three-dimensional finite-element modelling of Earth's viscoelastic deformation: Effects of lateral variations in lithospheric thickness. *Geophysical Journal International*, *155*(2), 679–695. https://doi.org/10.1046/j.1365-246X.2003.02084.x

Zhong, S., & Watts, A. B. (2013). Lithospheric deformation induced by loading of the Hawaiian Islands and its implications for mantle rheology. *Journal of Geophysical Research: Solid Earth*, *118*, 6025–6048. https://doi.org/10.1002/2013JB010408

Zhong, S., & Zuber, M. T. (2000). Long-wavelength topographic relaxation for self-gravitating planets and implications for the time-dependent compensation of surface topography. *Journal of Geophysical Research*, *105*, 4153–4164. https://doi.org/10.1029/1999JE001075

Zuber, M. T., Smith, D. E., Watkins, M. M., Asmar, S. W., Konopliv, A. S., Lemoine, F. G., … Wieczorek, M. A. (2013). Gravity field of the Moon from the Gravity Recovery and Interior Laboratory (GRAIL) mission. *Science*, *105*(E2), 4153–4164. https://doi.org/10.1029/1999JE001075

Formation of the lunar fossil bulges and its implication for the early Earth and Moon

Chuan Qin[1†], Shijie Zhong[1], and Roger Phillips[2]

[1]Dept. of Physics, Univ. of Colorado at Boulder, Boulder, CO 80309, USA.

[2]Dept. of Earth and Planetary Sciences and McDonnell Center for the Space Sciences, Washington Univ., St. Louis, MO, 63130, USA

† Now at Dept. of Earth and Planetary Sciences, Harvard University, Cambridge, MA 02138, USA.

Contents of this file

Introduction

The supporting information presents the theoretical development and validation of our computational method for lunar fossil bulge formation (text S1) and also a discussion on the effect of crustal compensation on the basin corrected gravitational potential anomalies (text S2). Figures S1 and S2 show additional results from different rheological models that are used for comparison and discussion in the main paper. Figure S3 shows benchmark results of our method against a finite element method.

Text S1.

Computational method for lunar bulge formation

We describe in detail our semi-analytical, time domain, and propagator matrix based method for solving the governing equations (1) – (3) with time-dependent viscoelastic rheology (4) and applied potential (8). The general strategy is to use a backward Euler method for time discretization of all the equations. The time-discretized equations are then expanded in spherical harmonics, and solved in spatial domain with the application of propagator matrix method. This method is similar to that used in post-glacial rebound studies (Zhong et al., 2003) and has seen applications in studies of planetary deformation (Hanyk et al., 1996; Kamata et al., 2012; Robuchon et al., 2010; Tobie et al., 2008).

1. Time discretization

We define the increments of displacement, gravitational potential, tidal-rotational potential and strain from time step $n-1$ to n, respectively, as

$$\boldsymbol{v}_n = \boldsymbol{u}_n - \boldsymbol{u}_{n-1}, \tag{S1}$$

$$\delta\varphi_n = \varphi_n - \varphi_{n-1}, \tag{S2}$$

$$\delta V_n = V_n - V_{n-1}, \tag{S3}$$

$$\Delta\boldsymbol{\varepsilon}_n = \boldsymbol{\varepsilon}_n - \boldsymbol{\varepsilon}_{n-1} = \frac{1}{2}(\nabla\boldsymbol{v}_n + \nabla^{\mathrm{T}}\boldsymbol{v}_n). \tag{S4}$$

The time derivatives of stress and strain can be approximated by

$$\dot{\boldsymbol{\sigma}}_n \approx \frac{\boldsymbol{\sigma}_n - \boldsymbol{\sigma}_{n-1}}{\Delta t_n} \tag{S5}$$

$$\dot{\boldsymbol{\varepsilon}}_n \approx \frac{\Delta\boldsymbol{\varepsilon}_n}{\Delta t_n}, \tag{S6}$$

2

respectively, where Δt_n is the time step.

Substituting (S1) – (S6) into (1) – (4), and using the following scaling,

$$\boldsymbol{v} = R_0 \boldsymbol{v}',\ t = \frac{\eta_0}{\mu_0} t',\ \boldsymbol{\sigma} = \mu_0 \boldsymbol{\sigma}',\ \mu = \mu_0 \mu',\ \eta = \eta_0 \eta',\ \varphi = 4\pi G \rho_0 R_0^2 \varphi', \tag{S7}$$

where R_0 is Moon's radius, μ_0 and η_0 are the reference shear modulus and viscosity, we obtain the corresponding equations at time step n in a non-dimensional form (dropping out the prime superscripts), as

$$\nabla \cdot \boldsymbol{v}_n = 0, \tag{S8}$$

$$\nabla \cdot \left[\boldsymbol{\sigma}_n + \zeta \rho_0 (\varphi_n + V_n - g u_r) \mathbf{I} \right] = 0, \tag{S9}$$

$$\nabla^2 \delta \varphi_n = 0, \tag{S10}$$

$$\boldsymbol{\sigma}_n = -\tilde{P}_n \mathbf{I} + 2\tilde{\eta}_n \Delta \boldsymbol{\varepsilon}_n + \alpha_n \boldsymbol{\sigma}_{n-1}, \tag{S11}$$

where ζ is a normalization coefficient and $\zeta = \dfrac{4\pi G \rho_0^2 R_0^2}{\mu_0}$. In (S11), particularly,

$\tilde{\eta}_n = \dfrac{\eta_n}{\tau_n + \Delta t_n}$, $\alpha_n = \dfrac{\tau_n}{\tau_n + \Delta t_n}$, $\tilde{P}_n = P_n + \alpha_n P_{n-1}$, in which $\tau_n = \dfrac{\eta_n}{\mu_n}$ is the normalized

Maxwell time; the last term represents the pre-stress. As a special case, when t=0 (or n=0), the pre-stress is zero and (S11) can be reduced to

$$\boldsymbol{\sigma}_n = -P_0 \mathbf{I} + 2\mu \boldsymbol{\varepsilon}_0, \tag{S12}$$

which describes the pure elasticity of the medium. Note that in (S9) and (S10), we already apply the incompressibility condition with constant density ρ_0 for the medium, hence the Eulerian density perturbation $\rho_1^E = 0$. The solution of (S10) can be expressed directly by the surface and CMB topography, as described in latter section.

We solve (S8) – (S11) for incremental deformation and gravitational potential at time step n. The final deformation or 'bulge' is the cumulative of the incremental deformation from all previous time steps, as

$$\boldsymbol{u}_n = \boldsymbol{v}_0 + \boldsymbol{v}_1 + \boldsymbol{v}_2 + \cdots + \boldsymbol{v}_{n-1} + \boldsymbol{v}_n.$$

(S13)

The final gravitational potential due to the deformation is

$$\varphi_n = \delta\varphi_0 + \delta\varphi_1 + \delta\varphi_2 + \cdots + \delta\varphi_{n-1} + \delta\varphi_n,$$

(S14)

which we solve in the main text for the size of the bulge. Such time discretization for viscoelastic deformation problem can also be found in a finite element formation for post-glacial rebound problem (Zhong et al., 2003). However, we solve these equations using a propagator matrix technique that is more efficient than numerical methods for a planetary mantle with 1-D viscosity and elastic structures as we assume here for the lunar mantle.

2. Propagator matrix method

We use a conventional technique called the propagator matrix method to solve (S8) – (S11) semi-analytically (Hager & Connell, 1989; Qin et al., 2014). In order to do so, the unknown variables in the equations need to be expanded in spherical harmonics to separate the radially dependent factors from the angular dependence. Here, we define a stress-related auxiliary variable $\mathbf{T}_n$ for convenience of formulation, as

$$\mathbf{T}_n = \boldsymbol{\sigma}_n - \alpha_n \boldsymbol{\sigma}_{n-1}.$$

(S15)

The incremental displacement, $\hat{r} \cdot \mathbf{T}_n$ and gravitational potential are expanded in spherical harmonics, respectively, as follows,

$$v_r^n = y_1^n Y_{lm}, \ v_\theta^n = y_2^n Y_{lm}^\theta, \ v_\phi^n = y_2^n Y_{lm}^\phi,$$

(S16)

4

$$T_{rr}^n = y_3^n Y_{lm}, \ T_{r\theta}^n = y_4^n Y_{lm}^\theta, \ T_{r\phi}^n = y_4^n Y_{lm}^\phi, \tag{S17}$$

$$\delta\varphi_n = y_5^n Y_{lm}. \tag{S18}$$

In this notation, $(v_r^n, v_\theta^n, v_\phi^n)$ and $(T_{rr}^n, T_{r\theta}^n, T_{r\phi}^n)$ denote radial, co-latitudinal and east-longitudinal components of incremental displacement and $\hat{r} \cdot \mathbf{T}_n$ in spherical coordinates, respectively. $Y_{lm} = Y_{lm}(\theta, \phi)$ is the spherical harmonic function, where l and m are harmonic degree and order, respectively. The derivatives of Y_{lm} are defined as

$$Y_{lm}^\theta = \frac{dY_{lm}}{d\theta}, \ Y_{lm}^\phi = \frac{1}{\sin\theta}\frac{dY_{lm}}{d\phi} . \tag{S19}$$

$y_1^n, y_2^n, \cdots, y_5^n$ are all r-dependent unknown factors that are to be solved.

In principle, Y_{lm} can be spherical harmonic of any degree and order, i.e., (l, m). However, in this study, we only consider the degree-2 tidal-rotational potential (forcing) as in equation (8). The time-discretized, non-dimensional form of (8) can be simplified as

$$V_n = \omega^n(r,t)Y_{20}, \tag{S20}$$

where ω^n is the potential magnitude at time step n (similarly, $\delta\omega^n$ is the magnitude of the differential potential δV_n). Furthermore, the total displacement, stress and gravitational potential can also be expressed in the expansion form, such that

$$u_r^n = z_1^n Y_{lm}, \ u_\theta^n = z_2^n Y_{lm}^\theta, \ u_\phi^n = z_2^n Y_{lm}^\phi, \tag{S21}$$

$$\sigma_{rr}^n = z_3^n Y_{lm}, \ \sigma_{r\theta}^n = z_4^n Y_{lm}^\theta, \ \sigma_{r\phi}^n = z_4^n Y_{lm}^\phi, \tag{S22}$$

$$\varphi_n = z_5^n Y_{lm}, \tag{S23}$$

where $(l, m) = (2, 0)$, and $z_1^n, z_2^n, \cdots, z_5^n$ are cumulative of $y_1^n, y_2^n, \cdots, y_5^n$, respectively, through n time steps.

5

Using the expansion form (S16) – (S18), the partial differential equations (PDEs)

(S8) – (S11) can be converted into a 4-by-4 linear system of ordinary differential

equations (ODEs), and rewritten into a matrix form

$$\frac{dX_n}{d\gamma} = A_n \cdot X_n,$$

(S24)

where $\gamma = \ln(r)$, X_n is a 4-by-1 solution vector at time step n and

$$X_n = [y_1^n, y_2^n, rZ^n, ry_4^n]^\mathrm{T}.$$

(S25)

A_n is a 4-by-4 matrix which relates to the material properties of the lunar mantle as well
as the harmonic degree of the forcing, and

$$A_n = \begin{bmatrix} -2 & L & 0 & 0 \\ -1 & 1 & 0 & \dfrac{1}{\tilde{\eta}_n} \\ 12\tilde{\eta}_n & -6L\tilde{\eta}_n & 1 & L \\ -6\tilde{\eta}_n & 2(2L-1)\tilde{\eta}_n & -1 & -2 \end{bmatrix},$$

(S26)

where $L = l(l+1) = 6$ since $l = 2$. In (S25), Z^n is a compound quantity that results from

the equation of motion (S9), and

$$Z^n = y_3^n + \zeta\rho_0(\delta\omega^n + y_5^n - gy_1^n) + \beta_n\zeta\rho_0(\omega^{n-1} + z_5^{n-1} - gz_1^{n-1}),$$

(S27)

where $\beta_n = 1 - \alpha_n$. Note that due to incompressibility of the lunar mantle, the

deformation-induced potential is directly related to the radial displacement at the surface

and the core-mantle boundary (CMB), as (Zhong & Zuber, 2000)

$$y_5^n = \frac{1}{2l+1}[r_b(\frac{r_b}{r})^{l+1}\Delta\rho_{0b}y_1^n(r_b) + r^l\Delta\rho_{0s}y_1^n(r_s)],$$

(S28)

$$z_5^{n-1} = \frac{1}{2l+1}[r_b(\frac{r_b}{r})^{l+1}\Delta\rho_{0b}z_1^{n-1}(r_b) + r^l\Delta\rho_{0s}z_1^{n-1}(r_s)],$$

(S29)

where $l = 2$ in this study, r_b and r_s are radii of the CMB and the surface, while $\Delta\rho_{0b}$ and

$\Delta\rho_{0s}$ are the positive density contrast across the CMB and the surface.

The propagator matrix method is favorable to solve (S24) given the simple linearity

of the equations. Assuming two points at r_1 and r_2 within a uniform material layer and

$r_2 > r_1$, the solution at r_2, $\boldsymbol{X}_n(r_2)$, can be obtained directly through

$$\boldsymbol{X}_n(r_2) = \boldsymbol{P}_n(r_2, r_1)\boldsymbol{X}_n(r_1),\tag{S30}$$

as long as the solution at r_1 has been determined, where $\boldsymbol{P}_n(r_2, r_1)$ is the propagator

matrix, and

$$\boldsymbol{P}_n(r_2, r_1) = \exp[\boldsymbol{A}_n(\gamma_2 - \gamma_1)].\tag{S31}$$

However, in order to implement propagator matrix method throughout the whole mantle,

the continuity conditions at any internal boundaries as well as the boundary conditions at

the surface and the CMB must be taken into account.

At any internal boundary, the displacement, gravitational potential, and the total stress

are continuous, that is

$$\left[y_1^n\right]_-^+ = \left[y_2^n\right]_-^+ = \left[y_5^n\right]_-^+ = 0,\tag{S32}$$

$$\left[z_1^n\right]_-^+ = \left[z_2^n\right]_-^+ = \left[z_3^n\right]_-^+ = \left[z_4^n\right]_-^+ = \left[z_5^n\right]_-^+ = 0,\tag{S33}$$

where $\left[\ \right]_-^+$ denotes the jump of the enclosed quantity from lower to upper boundary,

whereas Z^n (or y_3^n) and y_4^n (i.e., components of $\boldsymbol{T}_n$) are discontinuous across any jump

of material property. Specifically,

$$\left[Z^n\right]_-^+ = -\left[\alpha_n[z_3^{n-1} + \zeta\rho_0(\omega^{n-1} + z_5^{n-1} - gz_1^{n-1})]\right]_-^+,\tag{S34}$$

7

$$\left[y_4^n \right]_-^+ = -\left[\alpha_n z_4^{n-1} \right]_-^+ .$$

(S35)

The stress field satisfies the free surface condition

$$\hat{r} \cdot \boldsymbol{\sigma}_n^s = 0 ,$$

(S36)

and the frictionless CMB condition

$$\hat{r} \cdot \boldsymbol{\sigma}_n^b = -[\zeta \rho_c (V_n^b + \varphi_n^b - g_b u_{rn}^b)]\hat{r} ,$$

(S37)

where the superscripts s and b denotes surface and CMB, respectively, ρ_c is the density

of the fluid outer core. (S36) and (S37) lead to reduction of unknowns in the solution

vectors at the surface and the CMB, which are

$$\boldsymbol{X}_n^s = [y_1^n(r_s), y_2^n(r_s), r_s Z^n(r_s), 0]^{\mathrm{T}} ,$$

(S38)

and

$$\boldsymbol{X}_n^b = [y_1^n(r_b), y_2^n(r_b), r_b Z^n(r_b), 0]^{\mathrm{T}} ,$$

(S39)

respectively, together with four unknowns $y_1^n(r_s)$, $y_2^n(r_s)$, $y_1^n(r_b)$ and $y_2^n(r_b)$; while

$Z^n(r_s)$ and $Z^n(r_b)$ can be expressed by

$$Z^n(r_s) = \zeta \Delta \rho_{0s} \left([\delta \omega^n(r_s) + y_5^n(r_s) - g_s y_1^n(r_s)] + \beta_n^s [\omega^{n-1}(r_s) + z_5^{n-1}(r_s) - g_s z_1^{n-1}(r_s)] \right) \quad \text{(S40)}$$

and

$$Z^n(r_b) = -\zeta \Delta \rho_{0b} \left([\delta \omega^n(r_b) + y_5^n(r_b) - g_b y_1^n(r_b)] + \beta_n^b [\omega^{n-1}(r_b) + z_5^{n-1}(r_b) - g_b z_1^{n-1}(r_b)] \right), \quad \text{(S41)}$$

respectively, where $\Delta \rho_{0s} = \rho_0$ and $\Delta \rho_{0b} = \rho_c - \rho_0$.

Considering a one-dimensional numerical grid that divides the lunar mantle into N

material layers, with the grid points at $r_b, r_1, r_2, \cdots, r_{N-1}, r_s$, the unknown solution vectors

$\boldsymbol{X}_n^b$ and $\boldsymbol{X}_n^s$ can be linked by successive propagation of $\boldsymbol{X}_n^b$ to the surface across the N

layers, after corrections of discontinuities at the $N-1$ internal boundaries. Specifically,

8

$$X_n(r_1) = P_n(r_1, r_b)X_n^b,$$

$$X_n(r_2) = P_n(r_2, r_1)\{X_n(r_1) + C_n(r_1)\},$$

$$\vdots$$

$$X_n(r_k) = P_n(r_k, r_{k-1})\{X_n(r_{k-1}) + C_n(r_{k-1})\}, \quad \text{(S42)}$$

$$\vdots$$

$$X_n(r_s) = P_n(r_s, r_{N-1})\{X_n(r_{N-1}) + C_n(r_{N-1})\}.$$

Therefore,

$$X_n^s = P_n(r_s, r_b)X_n^b + \sum_{k=1}^{N-1} P_n(r_s, r_k)C_n(r_k), \quad \text{(S43)}$$

in which $C_n(r_k)$ is the discontinuity correction at r_k, and

$$C_n(r_k) = [0, 0, c_n^1(r_k), c_n^2(r_k)]^T, \quad \text{(S44)}$$

where

$$c_n^1(r_k) = -r_k\Delta\alpha_n(r_k)\{z_3^{n-1}(r_k) + \zeta\rho_0[\omega^{n-1}(r_k) + z_5^{n-1}(r_k) - gz_1^{n-1}(r_k)]\}, \quad \text{(S45)}$$

$$c_n^2(r_k) = -r_k\Delta\alpha_n(r_k)z_4^{n-1}(r_k), \quad \text{(S46)}$$

and $\Delta\alpha_n(r_k)$ is the jump of α_n across r_k.

Based on (S38) – (S41), (S43) can be written into a system of linear equations

$$M_n \cdot x_n = d_n, \quad \text{(S47)}$$

where

$$x_n = [y_1^n(r_s), y_2^n(r_s), y_1^n(r_b), y_2^n(r_b)]^T, \quad \text{(S48)}$$

$$M_n = \begin{bmatrix} 1 + h_1 p_{13} & 0 & -(p_{11} + h_2 p_{13}) & -p_{12} \\ h_1 p_{23} & 1 & -(p_{21} + h_2 p_{23}) & -p_{22} \\ h_3 + h_1 p_{33} & 0 & h_4 - (p_{31} + h_2 p_{33}) & -p_{32} \\ h_1 p_{43} & 0 & -(p_{41} + h_2 p_{43}) & -p_{42} \end{bmatrix}, \quad \text{(S49)}$$

$$
\boldsymbol{d}_n = \begin{bmatrix} h_5 p_{13} + q_1 \\ h_5 p_{23} + q_2 \\ h_5 p_{33} - h_6 + q_3 \\ h_5 p_{43} + q_4 \end{bmatrix},
\tag{S50}
$$

p_{ij}'s are elements of $\boldsymbol{P}_n(r_s, r_b)$, q_i's are elements of $\boldsymbol{Q}_n = \sum_{k=1}^{N-1} \boldsymbol{P}_n(r_s, r_k) \boldsymbol{C}_n(r_k)$, and

$h_1, h_2, \cdots, h_6$ are given by

$$
\begin{aligned}
& h_1 = \frac{1}{2l+1} \zeta r_b^{l+1} \Delta\rho_{0b} \Delta\rho_{0s}, \ h_2 = \zeta r_b \Delta\rho_{0b} (g_b - \frac{1}{2l+1} r_b \Delta\rho_{0b}), \\
& h_3 = \zeta \Delta\rho_{0s} (\frac{1}{2l+1} \Delta\rho_{0s} - g_s), \ h_4 = \frac{1}{2l+1} \zeta r_b^{l+2} \Delta\rho_{0b} \Delta\rho_{0s}, \\
& h_5 = -\zeta r_b \Delta\rho_{0b} \left[\delta\omega^n(r_b) + \beta_n^b [z_5^{n-1}(r_b) - g_b z_1^{n-1}(r_b)] \right], \\
& h_6 = \zeta \Delta\rho_{0s} \left[\delta\omega^n(r_s) + \beta_n^s [z_5^{n-1}(r_s) - g_s z_1^{n-1}(r_s)] \right].
\end{aligned}
\tag{S51}
$$

With (S8) – (S11) been reduced to (S49), the unique solution of $\boldsymbol{x}_n$ fully determines the

lunar bulge at each time step.

3. Validation of computational method

We design a set of simple test cases and compare solutions for these cases from our

method with those from a finite element method, CitcomSVE (Zhong et al., 2003). The

test results show that our computational method is valid. Furthermore, these test cases

also provide physical insights into the bulge formation process and the roles of

lithosphere and change in the applied potential.

In the first three test cases, the same (2,0) potential is used with a Heaviside function

time dependence, i.e., a constant potential applied at t=0 and thereafter, but these three

cases have different viscosity structures. In the first case, the mantle has a uniform

viscosity η_0 with no lithosphere. Before the potential is applied, the mantle is stress-free

everywhere and the surface topography is zero (i.e., no bulge). At t=0 when the potential

is suddenly applied, the Moon responds elastically with a small surface radial displacement that, if normalized, equals exactly to the degree-2 lunar tidal Love number $h_2 = 0.0409$. As time evolves, the normalized radial displacement h_2 (i.e., the bulge topography) increases as the lunar interior stress relaxes over a time scale of ~200t_m, and is 2.466 at t=400t_m (Figure S3a). For a homogeneous planet without a core, the radial displacement Love number $h_2 = 2.5$. Our test calculations show that as the core radius decreases, h_2 approaches 2.5, as expected. The result is in an excellent agreement with that computed from CitcomSVE which yields $h_2 = 2.448$ at t=400t_m (Figure S3a). The second test case differs from the first case only in having a 60-km thick elastic lithosphere. The lithosphere reduces the surface displacement or bulge size by more than a factor of two, because the lithosphere acts to support stress (Figure S3a). In the third case, the lithospheric thickness increases linearly with time from 0 at t = 0 to 60 km at 400 t_m, but otherwise the third case is identical to the first. For the third case, the radial displacement h_2 is between the first and second cases (Figure S3a). These results agree with those from CitcomSVE within 2% at any time (Figure S3a).

In the second set of cases (cases 4-7), we test the effects of decreasing the applied potential in models with different lithosphere structures. In these cases, we use the final stage of test case 1 when the bulge is already created with $h_2 = 2.466$ as the initial conditions at t=0, but we reduce the applied potential by a factor of two either gradually with time or instantaneously. Cases 4, 5 and 6 use the identical rheological structures to cases 1, 2 and 3, respectively, except for dropping the applied potential instantaneously at t=0. As expected, the bulge size or h_2 decreases with time on a time scale of ~200 t_m before stabilizing at some constant values (Figure S3b). In test case 7, the applied

potential decreases by a factor of two gradually as a linear function of time from t=0 to t=400t_m and is then kept as constant thereafter, while the lithosphere thickens in the same way as in case 6. For this case, the bulge decreases, following a similar trend to the applied potential (Figure S3b). The bulge size difference between cases 6 and 7 implies that the size of the lunar fossil bulge is controlled by the relative time scale of the two processes: lithospheric thickening and lunar orbital recession. We take it as our physical foundation for all of our analyses. Again, the results from our computational method for all these cases are in excellent agreement with those from CitcomSVE (Figure S3b).

4. Computational model, time and radial resolutions

Our models cover ~4×10^9 years of lunar history (or ~$10^6 t_m$, where $t_m = \eta_0/\mu$ is the Maxwell time and is ~5000 years for $\eta_0 = 10^{22}$ Pas and $\mu = 6.5 \times 10^{10}$ Pa), and this time duration is typically divided into ~3×10^5 time steps with non-uniform time increments Δt. In the early lunar history when the applied potential and mantle viscosity vary more rapidly, Δt is taken as 0.02t_m, while in the later lunar history when time variations are slower, Δt may increase to ~10t_m to improve the computational efficiency.

The lithosphere in the early lunar history is thin with its thickness from 0 to 10's km but is important for supporting the lunar bulge and stress. It is therefore essential to resolve the lithosphere in the models. In our standard model setup, the mantle including the lithosphere is divided into four macro-layers: the top 50 km, 50-150 km depth range, 150-450 km depth range, and 450 km-CMB depth range. These four macro-layers are further divided into 50, 50, 50 and 1 layers, respectively, from the top to bottom layers. That is, the top three macro-layers that may experience viscosity changes with time due to elastic thickness growth have a resolution of 1, 2 and 3 km, respectively. The bottom

macro-layer from 450 km to CMB always has a constant viscosity of η_0 and only needs one layer in our propagator matrix based method. Numerical resolution tests were done to show that the time and radial resolutions are more than sufficient for our lunar bulge model calculations.

It should be pointed out that even though conventional numerical models (e.g., finite element method) may work for viscoelastic deformation with time-dependent viscosity (Melosh et al., 2013; Zhong & Watts, 2013), it is extremely challenging computationally to use them at such high radial and time resolutions for 3×10^5 time steps as in the lunar bulge problem here.

Text S2.

Gravitational effect of lunar crustal compensation

In this study, we used basin corrected degree-2 gravity anomaly coefficients, C_{20} and C_{22}, as direct measure of the size of lunar fossil bulge (Keane and Matsuyama, 2014). However, C_{20} and C_{22} may also contain degree-2 gravity signal from lunar crustal thickness variations that cannot be completely removed by basin correction. A degree-2 crustal structure may result from early lunar thermal process such as tidal heating, as suggested by Garrick-Bethall et al., (2014). Yet, since tidal heating is significant only when the Earth-Moon distance is less than $25R_E$ (Garrick-Bethall et al., 2014) or t<100 Myr in our model (Figure 2a), the elastic thickness, T_e, would be very small (Figure 1c) such that the degree-2 crustal structure is likely to be largely compensated, leaving a relatively weak gravity signal. Here, we estimate an upper bound of the degree-2 gravity signal of crustal thickness variations through crustal compensation calculations. We find

that such effect, if existing, would be no more than 15% of the observed degree-2 gravitational potential anomaly, and our interpretation of C_{20} and C_{22} (Keane and Matsuyama, 2014) as being largely attributed to fossil bulge is valid.

We use both basin-corrected gravitational potential and topography anomalies from Garrick-Bethall et al. (2014) (GB) and gravitational potential anomalies from Keane & Matsuyama (2014) (KM) to estimate a crustal compensation effect. Because these two studies used different principal axis coordinate systems, it is not possible to combine these fields at the spherical harmonic coefficient level. This is also the major obstacle that prevents us from using both gravity and topography values for our fossil bulge analyses. However, since the power spectra of these quantities are invariant to axes rotation, we calculate the degree-2 powers of gravitational potential and topography anomalies each in their own frame of principal axes and to estimate the gravitational effect of crustal compensation.

The basin-corrected degree-2 gravitational potential and topography coefficients are summarized in Table S1, and these values are defined in gravity (KM) and topography (GB) reference frames of principal axis, respectively. We calculate the degree-2 powers for each set of coefficients by

$$W_l = \sum_{m=0}^{l} (\bar{C}_{lm}^2 + \bar{S}_{lm}^2), \tag{S52}$$

where l and m are spherical harmonic degree and order, respectively ($l=2$), and W_l is the power at degree l. $\bar{C}_{lm}$ and $\bar{S}_{lm}$ are the 4π-normalized coefficients of gravitational potential and topography anomalies. Here we define $W_{2,g1}$, $W_{2,g2}$, $W_{2,h}$, and $W_{2,c}$ to be the degree-2 powers with subscriptions standing for KM gravity, GB gravity, GB

topography and model gravity due to compensation of GB topography, respectively. Surprisingly, because the basin correction methodologies were quite different, we find that the resultant degree-2 gravitational potential powers from the two individual studies are almost the same (as expected for a single data set), i.e., $W_{2,g1}$=8.48×10^{-9} and $W_{2,g2}$ =8.30×10^{-9} for GB (their Table S6), differing by only ~2%. We use $W_{2,g1}$ gravity power to evaluate the effect of crustal compensation.

The gravitational potential anomalies produced by a compensated topography can be calculated at each harmonic (l, m) using the equation (Turcotte et al., 1981)

$$\bar{C}_{lm,c} = \frac{3\rho_c}{5\bar{\rho}} \frac{\bar{C}_{lm,h}}{R_0} \left[1 - D_l \left(1 - \frac{d}{R_0} \right)^{l+2} \right] \equiv K_l \bar{C}_{lm,h} , \qquad (S53)$$

where R_0 is the mean radius of the Moon, $\bar{\rho}$ and ρ_c are mean and crustal densities and are 3340 kg/m^3 and 2550 kg/m^3 respectively, d is the mean crustal thickness of 40 km of the present-day Moon, D_l is degree of compensation, and K_l is defined as a transfer coefficient and is dependent only on l. We note that this equation applies equally to harmonic coefficients $\bar{S}_{lm,h}$ and $\bar{S}_{lm,c}$. To find out the upper bound of crustal compensation effect, we may simply assume that the entire degree-2 topography (Table S1) is completely isostatically compensated at the Moho surface with D_l=1, and the corresponding gravity power is

$$W_{2,c} = \sum_{m=0}^{2} (\bar{C}_{2m,c}{}^2 + \bar{S}_{2m,c}{}^2) = K_2^2 \sum_{m=0}^{2} (\bar{C}_{2m,h}{}^2 + \bar{S}_{2m,h}{}^2) = K_2^2 W_{2,h} . \qquad (S54)$$

The contribution of the crustal compensation to degree-2 basin corrected gravity field is characterized by $\gamma = \sqrt{W_{l,c} / W_{l,g1}}$, which is equal to 21% using the data from Table S1. This suggests that if all the degree-2 basin corrected topography is caused by crustal

compensation, it can only explain 21% of the observed degree-2 gravitational potential anomalies.

We may estimate the fossil bulge topography by scaling its present-day hydrostatic value. Using equation (8) for l=2 and m=0, the present-day hydrostatic bulge topography, $\bar{C}_{20,h\_hd} = -\frac{\sqrt{5}}{6g}\Omega^2 R_0^2 h_2 = -10$ m, taking Ω as the present-day's lunar spin rate, h_2=2.5 as radial displacement fluid Love number, and g=1.63 m/s^2. If we take the fossil bulge to be 15-20 times of the present-day hydrostatic value, $\bar{C}_{20,h\_hd}$, then the bulge topography at l=2 and m=0 may range from -150 to -200 meters, which accounts for 23-30% of the basin corrected topography at this harmonic (Table S1). This implies that 70-77% of the corrected topography may be compensated at the Moho or ~15% of the basin corrected gravitational potential anomalies may be due to the crustal compensation. We think that this would not significantly affect our fossil bulge interpretation of the basin corrected gravitational potential anomalies.

Table S1. Basin corrected degree-2 gravitational potential and topography coefficients which have 4π normalization (Wieczorek, 2007, eq. 3)

	Keane & Matsuyama (2014)	Garrick-Bethall et al. (2014)	
	Gravity ($\times10^{-5}$)[a]	Topography (km)[b]	Gravity ($\times10^{-5}$)[b]
$\bar{C}_{20}$	-6.98	-0.65	-4.3
$\bar{C}_{22}$	6.01	0.51	3.9
$\bar{C}_{21}$	—	—	3.7
$\bar{S}_{21}$	—	—	-5.9
$\bar{S}_{22}$	—	—	-0.9

[a] Defined in gravity reference frame of principal axis.
[b] Defined in topography reference frame of principal axis.
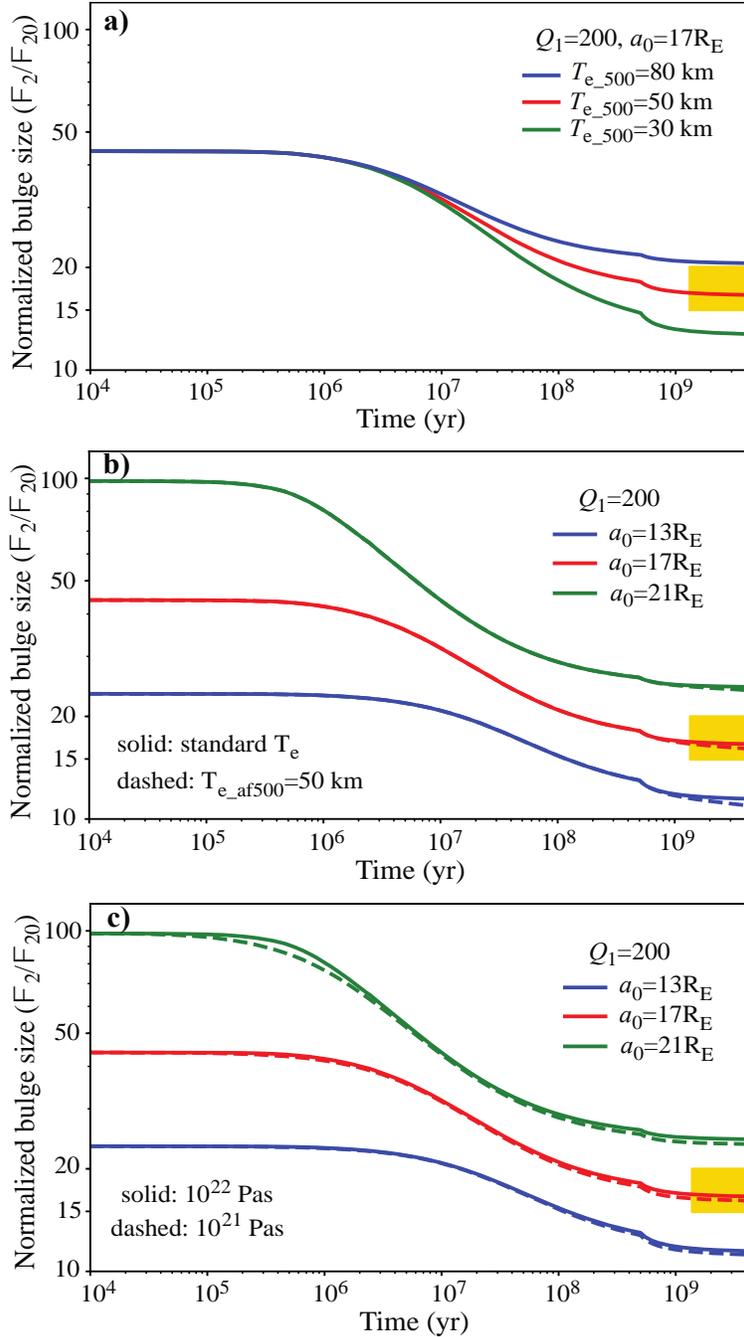
Figure S1. Time evolution of lunar bulge sizes for different rheological models. **a)** For models with $Q_1=200$, $a_0=17R_E$ and three different T_e at 500 Myr, T_{e_500}: 30 km, 50 km and 80 km. Note that $T_{e\_500}=50$ km is used in the reference rheological model. In these calculations, T_e increases from 0 to T_{e_500} at 500 Myr as a function of square root of time and then to 150 km at the present-day as a linear function of time. **b)** For models with $Q_1=200$ and three different a_0 using the reference rheological model (solid curves, which are the same as in Figure 2C) and a rheological model in which T_e is kept unchanged at 50 km from 500 Myr to the present-day (dashed curves). **c)** For models with $Q_1=200$ and three different a_0 using the reference rheological model (solid curves, which are the same as in Figure 2c) and a rheological model in which the mantle viscosity is 10^{21} Pas.

17
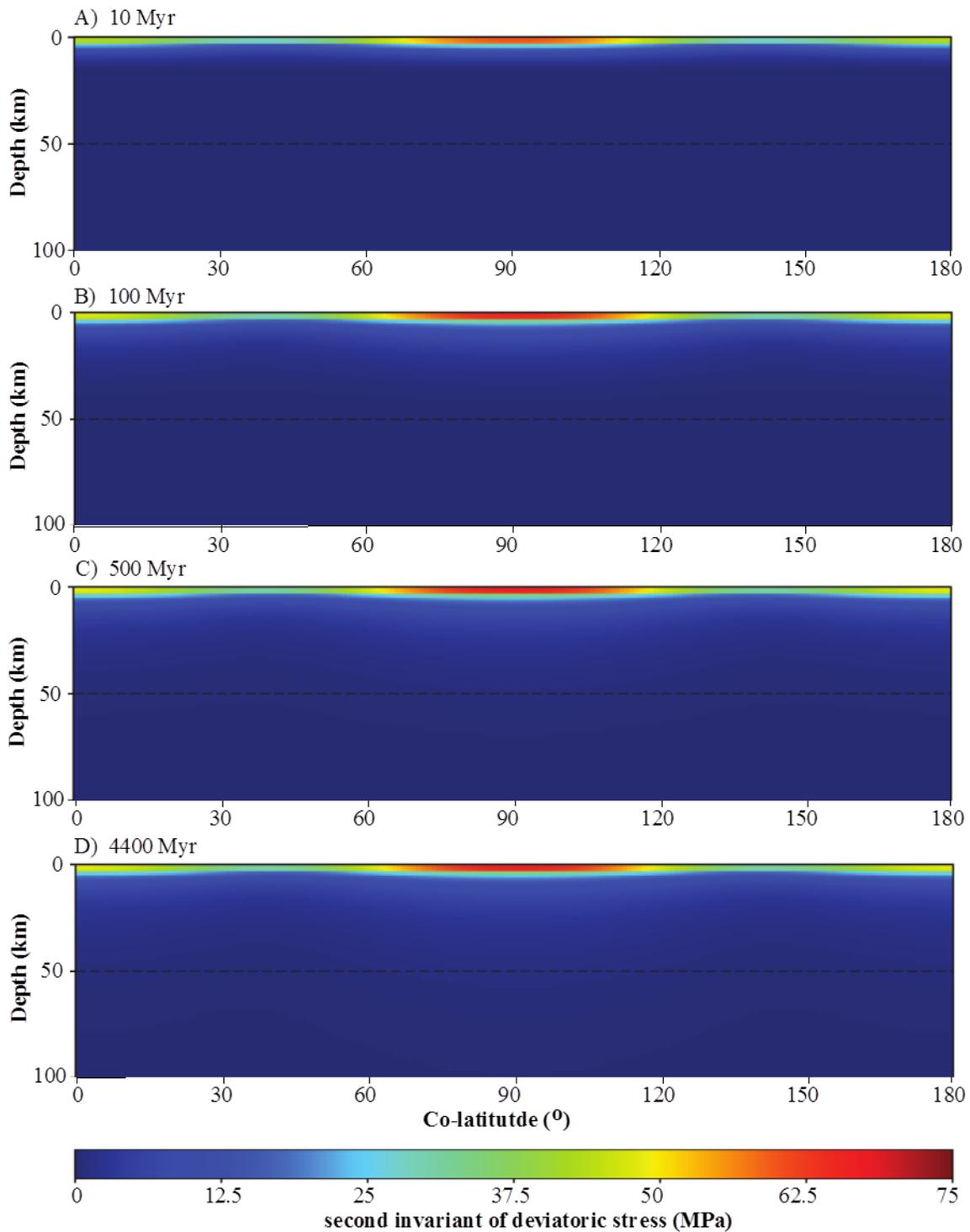
Figure S2. Spatial and temporal distribution of second-invariant of deviatoric stress for model with $Q_1=25$ and $a_0=11R_E$ that reproduces the observed bulges. a) The stress at different co-latitude (from 0 to 180°) for the top 100 km of the Moon at 10 Myr, **b)** 100 Myr, **c)** 500 Myr and **d)** 4.4 Gyr (or present-day). Note that the stress is concentrated at shallow depths and remains largely unchanged after the bulges are formed.

18
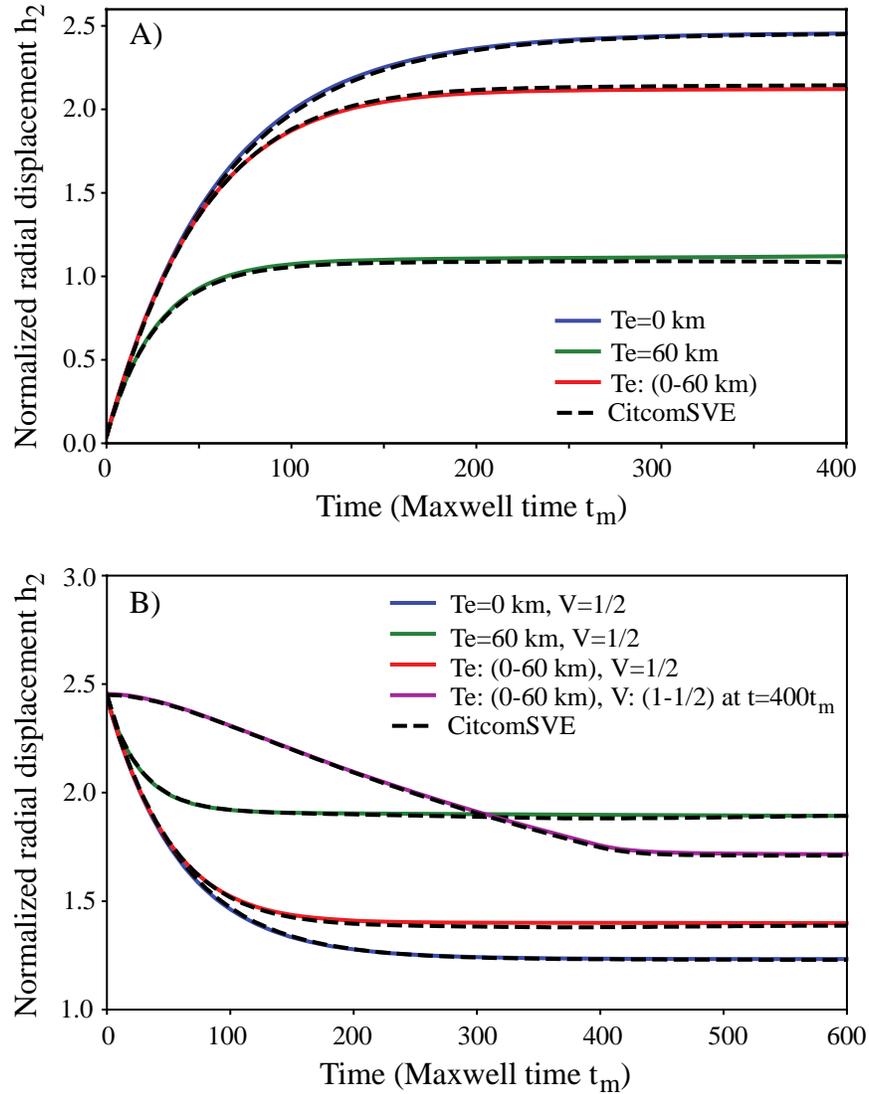
Figure S3. Validation of computational method for simplified models. a) Time evolution of normalized radial displacement for test cases 1 and 2 in which T_e is fixed as 0 and 60 km, respectively, and test case 3 in which T_e increases linearly from 0 at t=0 to 60 km at t=400t_m, where t_m is the Maxwell time. A constant potential at l=2 and m=0 is applied at t=0 and is kept thereafter (i.e., a Heaviside function or step function of time). **b)** Time evolution of normalized radial displacement for test cases 4-7 with different T_e and applied potential. For cases 4-7, model calculations start with the final bulge from test case 1 as initial conditions but with the applied potential reduced by a factor of 2 either instantaneously at t=0 (for cases 4-6) or gradually from t=0 to t=400t_m (for case 7). In both **a)** and **b)**, solid curves are from our new computational method, and dashed curves are from CitcomSVE. These two methods produce nearly the same results.